High-Speed Modeling of Ultracompact Electrooptic Modulators

Amirmahdi Honardoost , *Student Member, IEEE*, Reza Safian, Ashutosh Rao , *Student Member, IEEE*, and Sasan Fathpour , *Senior Member, IEEE, Fellow, OSA*

Abstract—The technology for compact thin-film lithium niobate electrooptic modulators has made significant advances recently. With achieving high levels of maturity for such platforms, a model is now required in order to accurately design the devices and reliably predict their performance limits. In this paper, a general transmission-line model is developed for predicting the frequency-dependent response of the compact modulators. The main radio frequency (RF) parameters of the modulators, such as characteristic impedance, effective index, and attenuation constant are calculated as a function of the coplanar waveguide dimensions, and validated by using numerical simulations. The accuracy of the model in predicting the 3-dB modulation bandwidth of the devices is verified by comparison with experimental results. Finally, guidelines for device design with significant improvement in the attainable modulation bandwidth are also presented by optimization of RF and optical parameters, predicting >100 GHz modulation bandwidth. The presented model is not limited to emerging thin-film lithium niobate devices, and is applicable to any type of ultracompact electrooptic modulator.

Index Terms—Electrooptic modulators, Thin-film lithium niobate, Transmission line modeling, Photonic integrated circuits.

I. INTRODUCTION

OPTICAL communication systems have been the focus of substantial amount of research over the past few decades [1], [2]. Optical modulators are among the key components of these systems for both digital and analog applications, such as optical interconnects, datacom and telecom, and integrated RF photonics [3]–[6]. Several platforms have been developed in order to pursue high-performance optical modulators.

A. Honardoost and S. Fathpour are with CREOL, the College of Optics and Photonics, University of Central Florida, Orlando, FL 32816 USA, and also with the Department of Electrical and Computer Engineering, University of Central Florida, Orlando, FL 32816 USA (e-mail: honardoost@knights.ucf.edu; fathpour@creol.ucf.edu).

R. Safian is with CREOL, the College of Optics and Photonics, University of Central Florida, Orlando, FL 32816 USA, and also with IMEC, Kissimmee, FL 34744 USA (e-mail: reza.safian@imec-int.com).

A. Rao is with CREOL, the College of Optics and Photonics, University of Central Florida, Orlando, FL 32816 USA (e-mail: ashutoshrao@knights.ucf.edu).

Color versions of one or more of the figures in this paper are available online at http://ieeexplore.ieee.org.
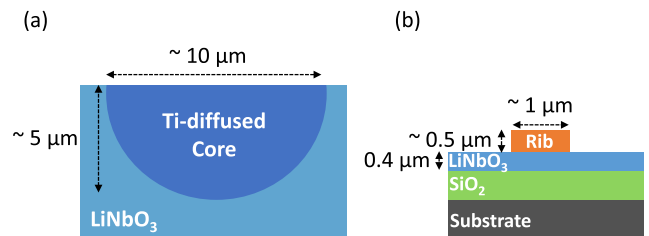
Fig. 1. (a) Conventional LN waveguide; (b) Compact thin-film LN waveguide.

Historically, commercial optical modulators have been made on materials with strong electrooptic (EO) effect (e.g., lithium niobate, LN or $LiNbO_3$) or electroabsorption (EA) effect (particularly, III–V compound semiconductors). More recently, silicon (Si) optical modulators based on free-carrier plasma dispersion effect (FCA) are being widely pursued, as they benefit from compatibility with standard Si foundry processing [6]–[8]. Another recent trend is heterogeneous integration of compound semiconductors as well as silicon germanium (SiGe), on silicon substrates that utilize EA effects such as Franz-Keldysh in bulk semiconductors or quantum-confined Stark effect in quantum-well structures [9]–[12]. Several modulators operating based on FCA or EA have been demonstrated with high data transmission rates up to 50 Gb/s. However, they typically suffer from low extinction ratios [9], [11]–[14].

On the contrary, modulators relying on linear EO or Pockel's effect have demonstrated modulation depth of 20 dB or more [15] as well as up to 100 GHz modulation bandwidth (BW) [16]. With such performance, LN has been well established as the standard material of choice for EO modulators in applications where high BW and extinction ratio are required, e.g., in long-haul communications [17]. Transparency in a broad range of the electromagnetic spectrum (0.4–5 μm), and a large EO coefficient (31 pm/V) are among other reasons which make LN a suitable option for EO modulators [15].

However, the conventional LN EO modulators suffer from a number of drawbacks, as proceeding to high integration levels is demanded. Two methods are traditionally used in order to form optical waveguides in conventional LN modulators, i.e., diffusion of dopants, such as titanium (Ti) [15], or the proton exchange process [18]. The resultant waveguides are generally several microns wide [19], [20], as shown in Fig. 1(a), and the refractive index contrast is relatively small ($\Delta n < 0.1$) [21] which leads to low optical confinement. Hence, the long Mach-

Zehnder (MZ) arm lengths, large half-wave voltage-length product ($V_\pi.l$), as well as high bending loss, restrict the exploitation of bulky LN EO modulators for desired large-scale photonic integration.

The heterogeneous integration of thin films of LN on oxidized Si substrates, has been recently demonstrated and pursued towards satisfying the requirement of large-scale integration, e.g., compact waveguide cross-sections, and low bending loss [22]. Our method has been to load the LN thin films with a rib waveguide made out of a refractive-index-matched material (such as tantalum pentoxide (Ta_2O_5) [22], chalcogenide glass (ChG) [23], or silicon nitride (Si_3N_4) [24]–[27]) in order to circumvent the LN etching issues and the associated high loss. It should be noted that low-loss LN etching has been recently demonstrated on LN thin films [28], [29]. Our team has also recently exploited direct etching of thin-film LN for highly efficient nonlinear-optic applications [30]. In any case, high optical confinement and low bending loss have been achieved by rib loading or direct etching, and as shown in Fig. 1(b), typical waveguide core dimensions have been significantly reduced by almost 30 times, i.e., from $\sim 2 \times 6~\mu m^2$ for half-intensity widths in conventional LN waveguides [20] to $0.4 \times 1~\mu m^2$.

As a result of these submicron waveguides, the gap between the electrodes of the MZ modulator can be decreased significantly compared to the conventional LN devices without introducing additional loss due to absorption of the optical mode by metallic electrodes. By utilizing this platform, we have previously demonstrated compact thin-film LN MZ EO modulators on Si substrates with a 3-dB modulation BW of 33 GHz and operating up to 50 GHz [24].

Compact LN modulators are not limited to the rib-loading and thin-film method described above. A variety of other approaches have been pursued [31]–[39]. A detailed review of different approaches and advances in thin-film LN modulator technology is beyond the scope of this work and has been recently published [40].

With achieving this level of maturity for these emerging platforms, an accurate model is now required in order to design high-performance devices and predict their performance limits. Despite some early work in recognizing the effect of frequency-dependent impedance mismatch in travelling-wave EO modulator [41], the commonly employed models in the literature for conventional LN modulators do not consider this effect. In these models, impedance matching is typically assumed between the MZ EO modulator's transmission line characteristics and the terminating resistive load at all frequencies [42], [43].

In this paper, we report on a much improved model in order to design, analyze and optimize the optical and RF device parameters of these compact (submicron) LN EO modulators. Electrical-optical modeling of the modulator based on coupled-mode theory is presented in Section II. In Section III, RF transmission-line modeling and calculation of its parameters by utilizing COMSOL^{TM} simulations as well as conformal mapping technique is discussed. Moreover, calculations based on the transfer function which is developed by taking the impedance mismatch between the transmission line and the terminating load into account, are presented.
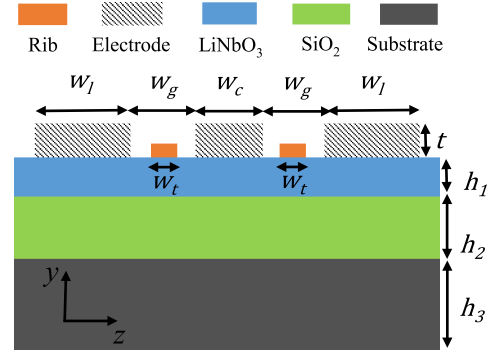

Fig. 2. Two dimensional schematic of a typical thin-film LN MZ EO modulator.

Simulation results are presented in Section IV, and design guidelines are discussed. By comparing the developed model with experimental results, the accuracy of the model in predicting the frequency-dependent response of the EO modulators is verified. In addition, design optimizations for both RF and optical parameters of the EO modulator are investigated. The results predict significant improvement in the 3-dB BW of such devices. Finally, concluding remarks are given in Section V.

II. ELECTRICAL-OPTICAL MODELING

Fig. 2 depicts the schematic cross-section of a generic thin-film LN MZ modulator in the push-pull configuration. The slab region of the optical waveguide is a *X*- or *Y*-cut thin-film of LN bonded to a layer of SiO_2 on silicon or LN substrate. As mentioned before, the thin-film LN is rib-loaded with an index-matched material, or directly etched, to provide lateral confinement for the optical mode. The applied RF electric field is aligned along the *z*-axis of LN. Hence, the strongest EO coefficient of LN crystal, i.e., $r_{33} \simeq 31$ pm/V [44], will be efficiently utilized.

Although this paper chooses the structure shown in Fig. 2 as a working example, the model developed here is more general and, in principle, can be applied to the other aforementioned compact LN platforms [31]–[39].

Based on Fig. 2, the effective refractive index along the *z*-direction is

$$n_z = n_e + \Delta n, \tag{1}$$

$$\Delta n = -n_e^3 r_{33} E_z^{RF}/2, \tag{2}$$

where n_e is the extraordinary refractive index of LN, and E_z^{RF} is the total electric field applied along the z direction. Based on the coupled-mode theory, the change in the amplitude of the optical field inside the waveguide can be calculated as

$$E_z^{op}(x) = E_z^{op}(0)e^{-j\tilde{C}_{11}x}, \tag{3}$$

where superscript *op* indicates the optical field, $\tilde{C}_{11}$ is the complex self-coupling coefficient defined as [44]

$$\tilde{C}_{11} = \Delta\tilde{\beta}_{op} = \omega_{op} \frac{\iint_S \Delta\tilde{\epsilon}(y,z)(\mathbf{E}_t^{op}.\mathbf{E}_t^{op*})ds}{\iint_S \hat{\mathbf{u}}_x.(\mathbf{E}_t^{op*} \times \mathbf{H}_t^{op} + \mathbf{E}_t^{op} \times \mathbf{H}_t^{op*})ds}, \tag{4}$$

and $\mathbf{E}_t^{op}$ and $\mathbf{H}_t^{op}$ are the transverse electric and magnetic field components of the optical wave propagating across the transverse surface S of the optical waveguide. $\hat{\mathbf{u}}_x$ is the unit vector along the direction of wave propagation. $\tilde{\epsilon}$ is the complex permitivity of the optical waveguide, and $\tilde{\beta}_{op}$ is the complex phase constant of the optical wave. Since

$$\tilde{\epsilon} = \epsilon_0 \tilde{n}^2, \tag{5}$$

and with $\tilde{n} = n + jn'$, the change in the permitivity is

$$\Delta\tilde{\epsilon} \approx 2n\epsilon_0 \Delta n, \tag{6}$$

if the perturbation of the imaginary part of the refractive index is ignored. Then, equation (4) can be written as

$$\Delta\tilde{\beta}_{op} = \omega_{op} \frac{\iint_S 2n\epsilon_0 \Delta n(\mathbf{E}_t^{op}.\mathbf{E}_t^{op*})ds}{\iint_S \hat{\mathbf{u}}_x.(\mathbf{E}_t^{op*} \times \mathbf{H}_t^{op} + \mathbf{E}_t^{op} \times \mathbf{H}_t^{op*})ds}. \tag{7}$$

For TE polarization

$$\iint_S \hat{\mathbf{u}}_x.(\mathbf{E}_t^{op*} \times \mathbf{H}_t^{op} + \mathbf{E}_t^{op} \times \mathbf{H}_t^{op*})ds$$
$$= \frac{2\beta_{op}}{\omega_{op}\mu_0} \iint_S \mathbf{E}_t^{op}.\mathbf{E}_t^{op*}, \tag{8}$$

and

$$\Delta\tilde{\beta}_{op} = \frac{-k_0^2 r_{33} n_e^4 \iint_S E_z^{RF}(\mathbf{E}_t^{op}.\mathbf{E}_t^{op*})ds}{2\beta_{op} \iint_S \mathbf{E}_t^{op}.\mathbf{E}_t^{op*}ds}. \tag{9}$$

Since we have neglected the change in the imaginary part of the refractive index, $\Delta\tilde{\beta}_{op}$ is approximately a real value, expressed as

$$\Delta\beta_{op} = \Delta n_{op}^{eff} k_0, \tag{10}$$

where k_0 is the vacuum wavenumber. By using equation (2) and (7), the perturbation to the optical effective index is

$$\Delta n_{op}^{eff} = \frac{-k_0 n_e^4 r_{33} \iint_S E_z^{RF}(\mathbf{E}_t^{op}.\mathbf{E}_t^{op*})ds}{2\beta_{op} \iint_S \mathbf{E}_t^{op}.\mathbf{E}_t^{op*}ds}. \tag{11}$$

In general, the RF field can be written as

$$E_z^{RF}(y,z) = \frac{V}{d}f(y,z). \tag{12}$$

The voltage V is a DC voltage for the lumped modulators, and it is a time-varying signal for traveling-wave EO modulators. d is the distance between the two metallic electrodes. $f(y,z)$ is the normalized spatial distribution of the electric field applied at the optical waveguide transverse plane. By defining the overlap of the electrical and optical fields as

$$\Lambda = \frac{\iint_S f(y,z)(\mathbf{E}_t^{op}.\mathbf{E}_t^{op*})ds}{\iint_S \mathbf{E}_t^{op}.\mathbf{E}_t^{op*}ds}, \tag{13}$$

equation (11) can be written as

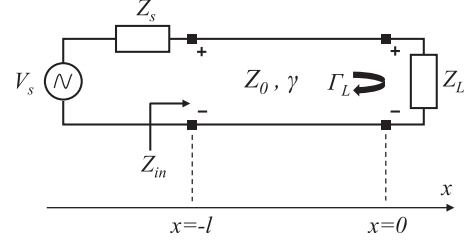$$\Delta n_{op}^{eff} = \Delta n_0 V, \ \Delta n_0 = \frac{-k_0 r_{33} n_e^4 \Lambda}{2\beta_{op}d}. \tag{14}$$

Fig. 3. Schematic of a general transmission line model. V_s is the source voltage with the impedance Z_S. The transmission line is terminated with a load with impedance Z_L. Z_0 and γ are characteristic impedance and complex propagation constant of the transmission line, respectively. The transmission line is along the x-axis.

III. RF TRANSMISSION LINE MODELING

As shown schematically in Fig. 2, the RF transmission line employed in the EO modulators is a symmetric coplanar waveguide (CPW) structure [15]. The signal is applied to the middle conductor and the other two conductors are ground planes (Ground-Signal-Ground (GSG) configuration). The main transmission line parameters of a CPW structure are the characteristic impedance (Z_0), attenuation constant (α_{RF}) and effective phase constant (β_{RF}). The standard lumped-element model of a transmission line [45] can be used to model the RF performance of the travelling-wave EO modulator, as depicted in Fig. 3. γ is the complex propagation constant, Z_0 is the characteristic impedance of the transmission line, and Z_{in} is the input impedance seen at the input of the transmission line with length l. Γ_L is the reflection coefficient due to the mismatch between Z_0 and the terminating resistive load (Z_L), and is defined as [45]

$$\Gamma_L = \frac{Z_L - Z_0}{Z_L + Z_0}. \tag{15}$$

Based on general transmission line theory, the voltage at each point of the transmission line is

$$V(x) = V_0^+ e^{\gamma x} + V_0^- e^{-\gamma x} = V_0^+(e^{-\gamma x} + \Gamma_L e^{+\gamma x}). \tag{16}$$

The voltage at the beginning of the line is calculated as

$$V(-L) = V_0^+(e^{\gamma L} + \Gamma_L e^{-\gamma L}) = V_S \frac{Z_{in}}{Z_{in} + Z_S}. \tag{17}$$

Then, we can find V_0^+ in terms of the source voltage as

$$V_0^+ = V_S \frac{Z_{in}}{Z_{in} + Z_S} \frac{1}{e^{\gamma l} + \Gamma_L e^{-\gamma l}}. \tag{18}$$

In the ideal case, in which both source and load impedances are matched to the line impedance ($Z_L = Z_0$, $Z_{in} = Z_0$),

$$\Gamma_L = 0, V_0^+ = V_S \frac{Z_0}{Z_0 + Z_S}. \tag{19}$$

However, this ideal case is almost impossible to achieve in practice across a broad RF band, as discussed later in Section III. Hence, it is necessary to introduce the effect of the impedance mismatch into the modeling.

As derived in the Appendix, the frequency-dependent transfer function of any EO modulator is

$$H(\omega_{RF}) = \frac{Z_{in}}{Z_{in} + Z_S} \frac{1}{e^{\gamma l} + \Gamma_L e^{-\gamma l}}$$
$$\left[\frac{\sinh(Al/2)e^{-Al/2}}{A/2} + \Gamma_L \frac{\sinh(Bl/2)e^{-Bl/2}}{B/2} \right],$$
$$\tag{20a}$$

$$A = -\alpha_{RF} - j\omega_{RF}(n_{RF} - n_{op})/c, \tag{20b}$$

$$B = +\alpha_{RF} + j\omega_{RF}(n_{RF} + n_{op})/c. \tag{20c}$$

where n_{RF} and n_{op} are the RF and optical wave refractive indices, respectively.

Equation (20) accounts for the RF attenuation coefficient, the phase velocity mismatch of the RF and optical traveling waves and the impedance mismatch between Z_S and Z_0. Moreover, unlike the conventional models [43], the impedance mismatch between the transmission line and the terminating load for the operating range has been taken into account.

In comparison, the commonly employed model for predicting the RF frequency response of the EO modulators is [43]

$$H(\omega_{RF}) = \frac{Z_{in}}{Z_{in} + Z_S} e^{-\alpha_{RF} l/2}$$
$$\left[\frac{\sinh^2(\alpha_{RF} l/2) + \sin^2(\omega_{RF}(n_{RF} - n_{op})l/2c)}{(\alpha_{RF} l/2)^2 + (\omega_{RF}(n_{RF} - n_{op})l/2c)^2} \right]^{1/2}.$$
$$\tag{21}$$

In this conventional model, impedance matching between Z_0 and Z_L is assumed at all frequencies. As shown later in this work, this assumption is not valid for compact EO modulators, and leads to overestimation of the 3-dB BW. The comparison between these two approaches are presented in Section IV.

Next, the main parameters of the RF transmission line, i.e. Z_0, n_{RF}, and α_{RF} are calculated as follows.

A. Characteristic Impedance

The characteristic impedance of the modulator is calculated by using COMSOL^{TM} simulations. Based on the quasi-Transverse Electromagnetic analysis of the CPW structure, RF electric and magnetic fields (denoted by $\mathbf{E}_{RF}$ and $\mathbf{H}_{RF}$ respectively) are used to calculate the resistance (R), inductance (L), conductance (G), and capacitance (C) circuit parameters per unit length for the CPW structure. The standard elements are calculated as [45]

$$R = \frac{R_S}{I^2} \int_l \mathbf{H}_{RF}.\mathbf{H}_{RF}^* dl, \quad L = \frac{\mu_0}{I^2} \int_S \mathbf{H}_{RF}.\mathbf{H}_{RF}^* ds,$$
$$G = \frac{\omega_{RF} \epsilon''}{V^2} \int_S \mathbf{E}_{RF}.\mathbf{E}_{RF}^* ds, \quad C = \frac{\tilde{\epsilon}}{V^2} \int_S \mathbf{E}_{RF}.\mathbf{E}_{RF}^* ds$$
$$\tag{22}$$

where R_S is the surface resistance of the metal electrodes, ϵ'' is the imaginary part $\tilde{\epsilon}$, V is the potential difference between the CPW electrodes, and I is the current flowing in the electrode.

Then, the frequency-dependent Z_0 is calculated as

$$Z_0 = \sqrt{\frac{R + j\omega_{RF} L}{G + j\omega_{RF} C}}. \tag{23}$$

The characteristic impedance of a CPW with a GSG configuration and multilayered substrate can be also obtained by using the conformal mapping technique as [46]

$$Z_0 = \frac{K'(k)}{4\epsilon_0 c K(k)\sqrt{\epsilon_{RF}^{eff}}}, \tag{24}$$

where c is the velocity of electromagnetic waves in free space, ϵ_{RF}^{eff} is the effective dielectric constant of the transmission line and $k = x_a/x_b$, where $x_a = W_c/2$, $x_b = W_c/2 + W_g$, $x_c = W_c/2 + W_g + W_l$. $K(\cdot)$ and $K'(\cdot)$ are the complete elliptic integrals of the first kind and its complement, respectively. The effective dielectric constant is

$$\epsilon_{RF}^{eff} = 1 + \sum_1^3 q_i, \tag{25}$$

where q_i is the filling factor, and 1, 2, and 3 correspond to LN, SiO$_2$ bottom cladding and substrate layers, respectively, as shown in Fig. 2. For $i = 1$ and 2, q_i is defined as [46], [47]

$$q_i = \frac{1}{2}(\epsilon_{r,i} - \epsilon_{r,i+1})\frac{K(k)K(k_i')}{K(k')K(k_i)}, \tag{26}$$

where

$$k_i = \frac{\sinh(\pi x_c/2h_i)}{\sinh(\pi x_b/2h_i)}\sqrt{\frac{\sinh^2(\pi x_b/2h_i) - \sinh^2(\pi x_a/2h_i)}{\sinh^2(\pi x_c/2h_i) - \sinh^2(\pi x_a/2h_i)}},$$
$$k_i' = \sqrt{1 - k_i^2}, \tag{27}$$

and for the substrate layer

$$q_3 = \frac{1}{2}(\epsilon_{r,3} - 1)\frac{K(k)K(k_3')}{K(k')K(k_3)}, \tag{28}$$

where

$$k = \frac{x_c}{x_b}\sqrt{\frac{x_b^2 - x_a^2}{x_c^2 - x_a^2}}, \quad k' = \sqrt{1 - k^2}. \tag{29}$$

The frequency variation of the ϵ_{RF}^{eff} is calculated as

$$\epsilon_{RF}^{eff}(f) = \left[\sqrt{\epsilon_{RF}^{eff}(0)} + \frac{\sqrt{\epsilon_r} - \sqrt{\epsilon_{RF}^{eff}(0)}}{1 + G(f/f_{TE})^{-1.8}} \right]^2, \tag{30}$$

where

$$G = \exp(u \ln(W_c/W_g) + v),$$
$$u = 0.54 - 0.64p + 0.015p^2,$$
$$v = 0.43 - 0.86p + 0.54p^2,$$
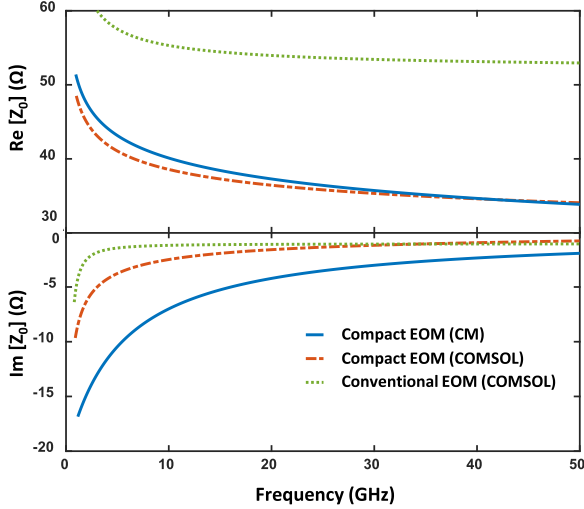$$p = \ln(W_c/h),$$
$$f_{TE} = c/4h\sqrt{\epsilon_r - 1}, \tag{31}$$

Fig. 4. Comparison between the calculated real part, and imaginary part of the characteristic impedance (Z_0) of the example electrooptic modulator (EOM) using conformal mapping (CM) and COMSOL™ simulations vs. the conventional bulk modulator for the operating frequency range.
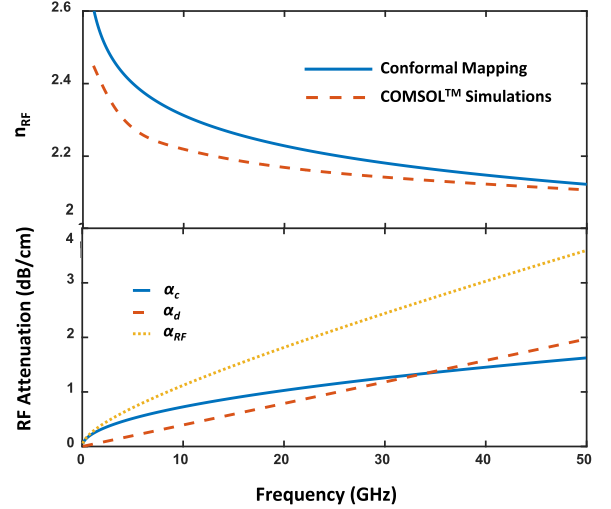

Fig. 5. Calculated RF refractive index (n_{RF}) of the example modulator using conformal mapping and COMSOL™ simulations, and α_c, α_d, and α_{RF} by using conformal mapping method.

and $h = h_1 + h_2 + h_3$ in the current structure and $\epsilon_r = \sum_{i=1}^{3} \epsilon_{r,i}/3$. It is worth mentioning that the values of the characteristic impedance and the effective permittivity obtained here are valid for infinitesimally thin CPW metallic strip conductors. As shown in Fig. 2, in practice, the metallization has a finite thickness t that affects the characteristics. It has been observed that as the metal thickness is increased, characteristic impedance and effective permittivity are both decreased consequently, but in the case $t/w_c << 1$, the effect of metal thickness can be neglected [46].

The structure shown in Fig. 2 is used as an example with $l = 8$ mm. The characteristic impedance of the modulator with dimensions $W_g = 5.5$ μm, $W_c = 12$ μm, $W_l = 8.5$ μm, $W_t = 1.2$ μm, $t = 2$ μm, $h_1 = 400$ nm, $h_2 = 2$ μm, and $h_3 = 500$ μm for Si substrate is calculated using COMSOL™ simulations and the conformal mapping method described above with calculated filling factors of 0.35, 0.01, and 0.001 for q_1, q_2, and q_3, respectively, for Si substrate. For the case of LN substrate, $\epsilon_{r,3}$ in Eq. (28) is about three times higher than that of Si, but q_3 is still a small factor. The results agree with negligible difference, i.e., ~5% of each other (For example $Z_0 = 48.38$ Ω using COMSOL™ simulations (Eq. (23)), and $Z_0 = 50.7$ Ω calulated using the conformal mapping method (Eq. (24)), both calculated at 1 GHz frequency). The trends versus RF frequency (0 to 50 GHz) are presented in Fig. 4, and Fig. 5 for Z_0 and n_{RF}, respectively.

It is evident that the Z_0 of the compact modulator in the example varies from ~ 50 Ω to ~ 35 Ω as the frequency is increased from DC to 50 GHz, whereas the characteristic impedance of the conventional bulk LN modulators remains almost invariant for the most part of the operating frequency range [48]. This is confirmed through our COMSOL™ simulations by using structure in Fig. 2 with $W_g = W_l = W_c = 20$ μm, and $t = 5$ μm on bulk LN substrate which resembles a typical conventional LN modulator. Shown also in Fig. 4, this clearly shows the impor-

tance of impedance matching between the modulator and the terminating load, in the case of the compact modulators.

B. RF Attenuation Constant

The RF attenuation constant is another important design parameter which should be carefully studied. As discussed later in Section IV, it plays an important role in predicting the frequency response of the EO modulator and its BW. The attenuation constant of the CPW structure is generally defined as

$$\alpha_{RF} = \alpha_c + \alpha_d + \alpha_r, \tag{32}$$

where α_c is the ohmic or metalic conductor attenuation constant, α_d is the dielectric attenuation constant and α_r is the radiation attenuation constant. The dimensions of α_c, α_d and α_r are dB per unit length. Here, with smooth metal deposition for electrodes, α_r is neglected. The expressions for the attenuation constant due to dielectric loss in CPW structure is the same as that for a microstrip, which is [46]

$$\alpha_d = \frac{2.73}{c} \frac{\epsilon_r}{\sqrt{\epsilon_{RF}^{eff}}} \frac{\epsilon_{RF}^{eff} - 1}{\epsilon_r - 1} (\tan \delta) f, \tag{33}$$

where $\tan \delta$ is called the dielectric loss tangent, and it is taken from [49], [50], and [51] for SiN, LN, and SiO$_2$, respectively.

The ohmic loss is calculated by evaluating the power dissipated in the line through conformal mapping of the current density in the finite metal thickness structure [52] as $\alpha_c = \alpha_{c0} \sqrt{f}$, where α_{c0} is defined as

$$\alpha_{c0} = \frac{R_{s0} \sqrt{\epsilon_{RF}^{eff}}}{480\pi K(k) K'(k)(1-k^2)} \left[\frac{1}{x_b} \left(\pi + \ln \left(\frac{8\pi x_a (1-k)}{t(1+k)} \right) \right) \right.$$
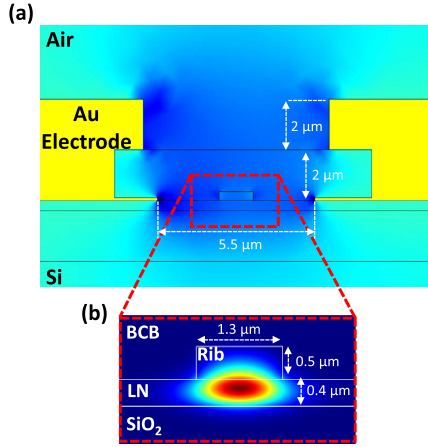$$\left. + \frac{1}{x_b} \left(\pi + \ln \left(\frac{8\pi x_b (1-k)}{t(1+k)} \right) \right) \right], \tag{34}$$

Fig. 6. (a) Simulated RF mode profile of MZ modulator with 5.5 μm gap between the electrodes at 10 GHz.; (b) Simulated optical mode profile of the hybrid ridge waveguide with Si_3N_4 rib.

where R_{s0} is the surface resistance of the strip conductor at low frequencies. The transformation rule used for calculating elliptic integrals is

$$K(k) = (1 + k_s)K(k_s), K(k') = \frac{1 + k_s}{2}K(k'_s), \quad (35)$$

where

$$k_s = x_a/x_b, k'_s = \sqrt{1 - k_s^2}, k = \frac{2\sqrt{k_s}}{1 + k_s}, k' = \frac{1 - k_s}{1 + k_s}. \quad (36)$$

The RF attenuation and both parts of it, i.e., α_c and α_d, are depicted in Fig. 5 for the example modulator discussed in the previous section $l = 8$ mm. Clearly, α_d cannot be neglected at high frequencies.

IV. SIMULATION RESULTS AND DISCUSSIONS

RF and optical mode profiles of the EO modulator structure of Fig. 2 are simulated using COMSOL^{TM} and presented in Fig. 6. In this structure, more than 70% of the optical mode is confined within the LN thin film for Si_3N_4 rib with an index of 1.93 at 1550 nm. The evident high lateral optical confinement compared to conventional LN devices allows for reduced electrode gaps of 5.5 μm, and reduction in device's overall footprint, without introducing additional absorption of the optical mode by metallic electrodes. Meanwhile, the high lateral confinement of the electric field in LN provides negligible optical loss at the sharp Y-junctions of the MZ modulator, and more importantly, a desired overlap of the RF and optical field, which leads to lower drive voltages compared to traditional bulky LN modulators, and consequently a lower $V_\pi.l$, which is an important figure of merit for EO modulators. By further increasing the optical mode overlap in LN, the drive voltage can be reduced. However, this simultaneously results in lower lateral confinement and can potentially increase the electrode-induced optical loss, and consequently degrades the overall performance of the device [40]. Therefore, this trade-off should be considered carefully in the design procedure.

It is observed that the effective refractive index of the optical waveguide plays an important role in the final RF performance
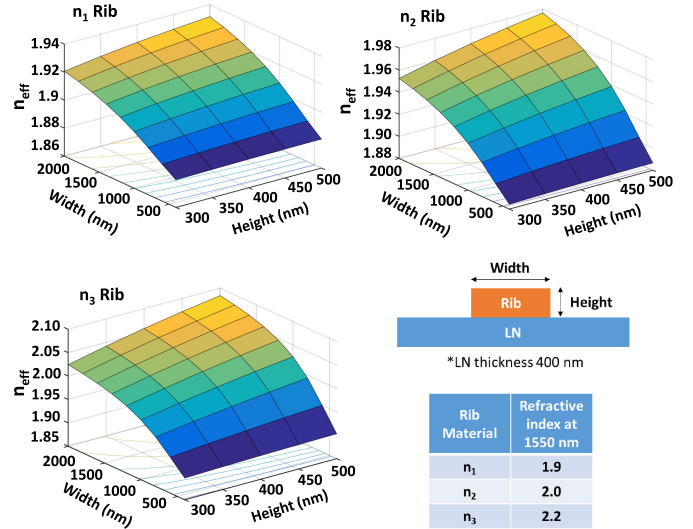

Fig. 7. Calculated effective refractive indices of optical waveguide of the modulator for 3 different rib-loading materials as examples. The height and width of the rib is varied. The thin-film LN thickness is 400 nm. The inset table shows the assumed refractive indices of rib-loading materials.

of the modulator, i.e., in the frequency-dependent velocity mismatch between the RF and optical modes (see Eq. (20)). Since the effective refractive index of the RF guided mode (n_{RF}) decreases with RF frequency, as depicted in Fig. 5, while the optical refractive index (n_{op}^{eff}) remains constant, the mismatch between these two indices should be minimized as much as possible, by using the n_{rib} value to tune n_{op}^{eff} (see Figs. 7 and 8(a)).

In order to study the range of achievable values for n_{op}^{eff}, the optical waveguide region of the compact EO modulator in Fig. 6 is simulated using COMSOL^{TM} and the results are presented in Fig. 7. The height and width of the rib is varied for three different rib-loading materials with optical refractive indices of $n_{rib} = 1.9$, 2.0, and 2.2, as an example (the case $n_{rib} = 2.2$ corresponds to LN). The height of the thin-film LN is fixed at 400 nm in the simulations. The acquired values for n_{op}^{eff} are utilized in Eq. (20) for $l = 8$ mm, and the EO frequency response of the modulator is depicted in Fig. 8(a). With the same waveguide cross-section, increasing n_{rib} results in higher BW and lower W_g, as observed in Fig. 8(a), and Fig. 8(b). For example, an all-LN platform, achieved by direct etching of LN ($n_{rib} = 2.2$) has higher BW compared to rib-loaded LN with rib indices lower than 2.2, while rib-loading with a material with a higher index of 2.3 would offer the highest BW.

It is evident that by employing the appropriate rib-loading material and optical waveguide dimensions, the 3-dB BW of the modulator can be improved significantly. It is observed that these degrees of freedom in using waveguide index, and dimensions are not easily attainable in traditional diffused LN modulators. As discussed later, the device length is also an important parameter, and 100 GHz BW is predicted with $l = 3$ mm (see Fig. 9(b)).

It should be noted that these simulation results are for the particular CPW electrode structure of Fig. 2. Other configurations for electrodes will vary the n_{RF} of the device and hence, require appropriate re-designing of the optical parameters. It
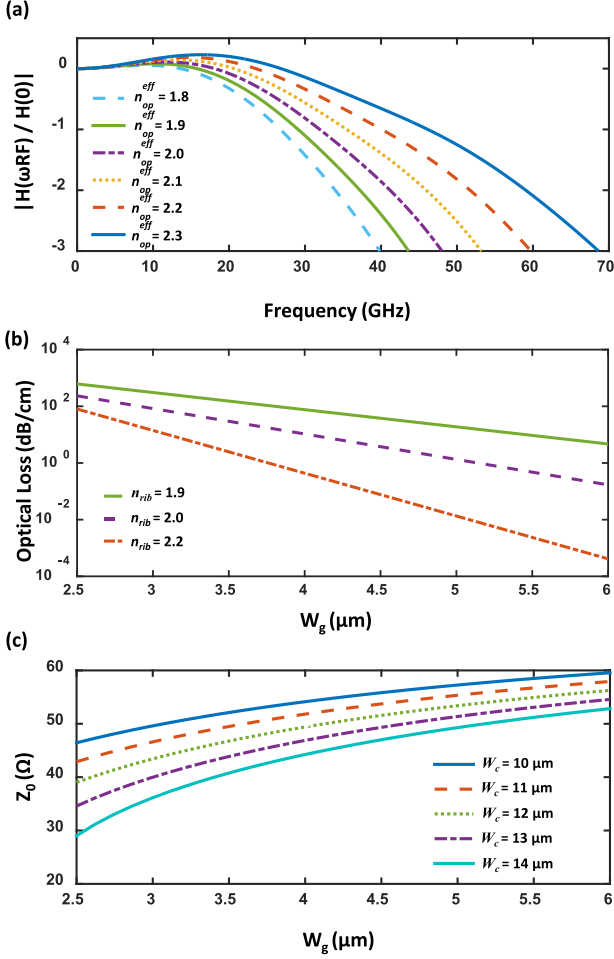
Fig. 8. (a) Variation of the normalized frequency dependent response of the EO modulator for different values of effective optical refractive index, n_{op}^{eff}.; (b) Simulated optical loss vs. the gap between the electrodes (W_g) for 3 different rib-loading materials as an example.; (c) Characteristic impedance (Z_0) vs. the gap between the electrodes (W_g) for different values of the center electrode's width (W_c).
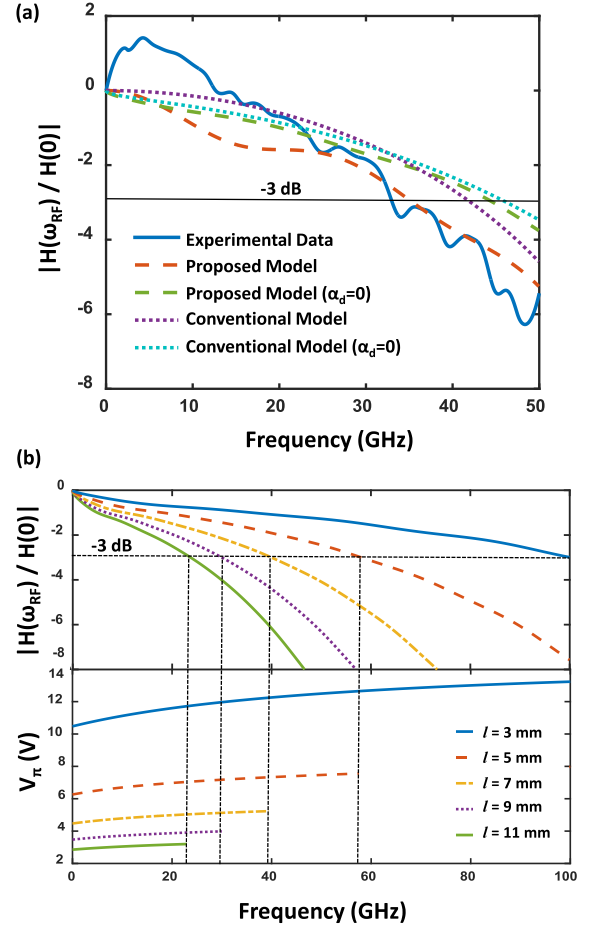

Fig. 9. (a) Comparison between the experimental data [24] vs. the performance prediction from the developed (see Eq. (20)) as well as the conventional model [43].; (b) Variation of the simulated frequency response, and half-wave voltage (V_π) of the modulators for different lengths of RF electrodes vs. the RF frequency.

is also important to mention that by changing the rib-loading material or the optical waveguide dimensions, the lateral confinement of the optical mode will vary. Therefore, the gap between the electrodes has to be designed accordingly in order to avoid the metal-induced additional loss.

Fig. 8(b) presents optical loss vs. W_g for different rib-loading materials to show the trade-off between loss and confinement. It is stressed that optical loss values only account for the metallic electrodes and ignore the material loss of LN and the rib-loading materials, as well as any fabrication-dependent sidewall scattering loss. Fig. 8(b) suggests that employing a rib-loading material with higher refractive index yields shorter gaps and consequently more compact and lower-voltage devices. With large enough W_g, metal-induced absorption loss is negligible, and the overall transmission of the EO modulator is maximized. Meanwhile, the optical propagation loss does not affect the frequency response of the modulator, and its 3-dB BW. On the other hand, the RF loss plays a key role in determining the performance limits of the modulator, and as mentioned before, it should be carefully studied.

Here, a comparison between the driving voltage of rib-loading versus direct etching of LN is presented. Directly-etched LN waveguides clearly have higher optical mode overlap with the active region and the mode is more confined. Also, with an index of 2.2 for LN, directly-etched devices can afford smaller W_g compared to $n_{rib} < 2.2$ for the same metallic loss. For example, the data in Fig. 8(b) suggests that for a loss of 1 dB/cm, $W_g = 3.7$ μm for $n_{rib} = 2.2$ (LN) and $W_g = 5.1$ μm for $n_{rib} = 2.0$. However, as also pointed out elsewhere [40], the RF electric field drops in both the rib and the LN active region, as the dielectric constant of the rib material increases. Consequently, the overlap of the electric and optical fields, Λ in Eq. 13, drops and to some extent counteracts the shorter W_g in $V_\pi.l$ calculations. For instance, in the same example described above, Λ is 64% for $n_{rib} = 2.2$ (LN) and 67% for $n_{rib} = 2.0$. Accordingly, the final $V_\pi.l$ values are 2.93 and 3.82 V.cm, respectively.

As discussed earlier, one important issue neglected in traditional models is the impedance mismatch between the characteristic impedance of the modulator (Z_0) and the terminating 50-Ω resistive load. This mismatch has been taken into account in our developed model as denoted by Γ_L in Eq. (20). While Z_0 varies with RF frequency, the CPW elecrodes structure of

the modulator is designed in such a way to maintain characteristic impedance as close as possible to 50 Ω. Fig. 8(c) shows the variation of Z_0 versus W_g for different widths of the center electrode, denoted by W_c in Fig. 2.

Finally, for the purpose of verification, the developed model is utilized to compare with the frequency-dependent response of a fabricated device in our previous work [24], i.e., the device with the cross-section shown in Fig. 6 and with $l = 8$ mm. As shown in Fig. 9(a), the proposed model follows the experimental data and is capable of accurately predicting the 3-dB BW of the modulator. However, it can be observed that the characterization data and the frequency response resulted from the developed model do not match at low frequencies. One possible reason is that the wavelength of the RF signal is much greater than the transverse dimensions of the EO modulator in this frequency range. Hence, the peripheral apparatus such as the metallic holders or the optical test bench below can potentially affect the measured RF response of the device. Since these parasitic elements are not considered in this model, the accuracy of the model at lower frequencies could have been compromised. Further investigation of this attribution requires more detailed modeling, which is beyond the scope of this work.

The discrepancy between the conventional [43] and the proposed model (see Eq. (20)) is clearly apparent in Fig. 9(a). The result from conventional modeling considerably overestimates the 3-dB BW of the modulator. It is also observed that if α_d is neglected in the models, the performance predictions are no longer valid.

Accurate calculation of RF loss and refractive index, as well as taking the mismatch between Z_0 and Z_L into account are both required in order to properly predict the frequency response of the compact EO modulators.

Finally, in order to further improve the 3-dB BW of the modulator, the optimized device length is studied. As shown in Fig. 9(b), shorter electrode lengths provide larger BW for the same designed structure of Fig. 6 [24], but with different l values. The results predict the potential for achieving 3-dB BW of 100 GHz for $l = 3$ mm. However, it should be noted that larger BW is attainable at the cost of increased half-wave voltage (V_π). The variation of V_π vs. RF frequency (DC to 3-dB BW) is depicted in Fig. 9(b) for different values of l.

V. Conclusion

In summary, we have developed a general transmission-line model that accurately predicts the frequency-dependent response of ultracompact (submicron) and high-speed electrooptic modulators. The major RF parameters of such devices are calculated as a function of coplanar waveguide dimensions. The design procedure of these compact modulators in terms of RF, as well as optical parameters are presented, and the model is utilized to analyze and optimize the high-speed performance of such devices. Finally, the accuracy of the model is verified by comparing the results with the characterization data obtained from fabricated devices. Unlike conventional models, the developed model presented in this work, is capable of accurately predicting the 3-dB bandwidth of ultracompact

LN EO modulators. By utilizing this model, and with proper design of such compact EO modulators, the 3-dB modulation bandwidth can be improved to >100 GHz, which is an important attribution for advanced optical communication systems.

Appendix

Formulations for calculating the proposed frequency-dependent transfer function of the EO modulator, Eq. (20), are developed in the following.

The complex propagation constant of the RF transmission line is defined as

$$\gamma = \alpha_{RF} + j\beta_{RF}. \tag{A1}$$

where the real part of the propagation constant, α_{RF}, is the attenuation constant and the imaginary part, β_{RF}, is the phase constant of the transmission line.

In general, the total phase shift of the optical field along the the electrode length l which the RF transmission line is presented is

$$\Delta\Phi_{op} = \Delta\Phi(\omega_{RF}, t) = \int_{-l}^{0} \Delta\beta_{op}dx, \tag{A2}$$

where $\Delta\beta_{op}$ is defined as

$$\Delta\beta_{op} = k_0\Delta n_{op}^{eff}. \tag{A3}$$

Then, using Eq. (14)

$$\Delta\beta_{op} = k_0\Delta n_0 V\left(x, t + \frac{x}{v_{op}^p}\right), \tag{A4}$$

where v_{op}^p is the phase velocity of the optical wave and is defined as

$$v_{op}^p = \omega_{op}/\beta_{op} = c/n_{op}^{eff}. \tag{A5}$$

The voltage of the transmission line in Fig. 3 which is time- and frequency-dependent can be written as

$$V\left(x, t + \frac{x}{v_{op}^p}\right) = V_0^+[e^{-\gamma x} + \Gamma_L e^{+\gamma x}]e^{j\omega_{RF}(t + x/v_{op}^p)}. \tag{A6}$$

If we define the transfer function, $H(\omega_{RF})$, via

$$\Delta\Phi_{op} = k_0\Delta n_0 H(\omega_{RF})e^{j\omega_{RF}t}V_S, \tag{A7}$$

then, $H(\omega_{RF})$ is

$$H(\omega_{RF}) = \int_{-l}^{0} V_0^+/V_S \left[e^{-\alpha_{RF}x}e^{-j\omega_{RF}(n_{RF}-n_{op})x/c}\right.$$
$$\left. + \Gamma_L\left(e^{-\alpha_{RF}x}e^{+j\omega_{RF}(n_{RF}+n_{op})x/c}\right)\right]dx. \tag{A8}$$

After integration, Eq. (20) is derived.

References

[1] D. Botez and G. J. Herskowitz, "Components for optical communications systems: A review," *Proc. IEEE*, vol. 68, no. 6, pp. 689–731, Jun. 1980.

[2] R. -J. Essiambre and R. W. Tkach, "Capacity trends and limits of optical communication networks," *Proc. IEEE*, vol. 100, no. 5, pp. 1035–1055, May 2012.

[3] D. A. B. Miller, "Optical interconnects to electronic chips," *Appl. Opt.*, vol. 49, no. 25, pp. F59–F70, 2010.

[4] L. A. Eldada, "Advances in telecom and datacom optical components," *Opt. Eng.*, vol. 40, no. 7, pp. 1165–1178, 2001.

[5] R. Williamson and R. Esman, "RF Photonics," *J. Lightw. Technol*, vol. 26, no. 9, pp. 1145–1153, May 2008.

[6] B. Jalali and S. Fathpour, "Silicon photonics," *J. Lightw. Technol.*, vol. 24, no. 12, pp. 4600–4615, Dec. 2006.

[7] G. T. Reed *et al.*, "Recent breakthroughs in carrier depletion based silicon optical modulators," *Nanophotonics*, vol. 3, no. 4/-5, pp. 229–245, 2014.

[8] R. A. Soref and B. R. Bennett, "Electrooptical effects in silicon," *IEEE J. Quantum Electron.*, vol. 23, no. 1, pp. 123–129, Jan. 1987.

[9] Y. Tang, H. -W. Chen, S. Jain, J. D. Peters, U. Westergren, and J. E. Bowers, "50 Gb/s hybrid silicon traveling-wave electroabsorption modulator," *Opt. Express*, vol. 19, no. 7, pp. 5811–5816, 2011.

[10] O. Qasaimeh, P. Bhattacharya, and E. T. Croke, "SiGe-Si quantum-well electroabsorption modulators," *IEEE Photon. Technol. Lett.*, vol. 10, no. 6, pp. 807–809, Jun. 1998.

[11] J. Liu *et al.*, "Waveguide-integrated ultralow-energy GeSi electro-absorption modulators," *Nat. Photon.*, vol. 2, pp. 433–437, 2008.

[12] S. Fathpour, "Emerging heterogeneous integrated photonic platforms on silicon," *Nanophotonics*, vol. 4, no. 1, pp. 143–164, 2015.

[13] X. Tu *et al.*, "50-Gb/s silicon optical modulator with traveling-wave electrodes," *Opt. Express*, vol. 21, no. 10, pp. 12776–12782, 2013.

[14] Y. Yang, Q. Fang, M. Yu, X. Tu, R. Rusli, and G. Lo, "High-efficiency Si optical modulator using Cu travelling-wave electrode," *Opt. Express*, vol. 22, no. 24, pp. 29978–29985, 2014.

[15] E. L. Wooten *et al.*, "A review of lithium niobate modulators for fiber-optic communications systems," *IEEE J. Sel. Quantum Electron.*, vol. 6, no. 1, pp. 69–82, Jan./Feb. 2000.

[16] K. Noguchi, O. Mitomi, and H. Miyazawa, "Millimeter-wave Ti:LiNbO₃ optical modulators," *IEEE J. Lightw. Technol.*, vol. 16, no. 4, pp. 615–619, Apr. 1998.

[17] M. Doi, M. Sugiyama, K. Tanaka, and M. Kawai, "Advanced LiNbO₃ optical modulators for broadband optical communications," *IEEE J. Sel. Top. Quantum Electron.*, vol. 12, no. 4, pp. 745–750, Jul./Aug. 2006.

[18] J. L. Jackel, C. E. Rice, and J. J. Veselka, "Proton exchange for high-index waveguides in LiNbO₃," *Appl. Phys. Lett.*, vol. 41, no. 7, pp. 607–608, 1982.

[19] P. G. Suchoski, T. K. Findakly, and J. Leonberger, "Stable low-loss proton-exchanged LiNbO₃ waveguide devices with no electro-optic degradation," *Opt. Lett.*, vol. 13, no. 11, pp. 1050–1052, 1988.

[20] M. Fukuma and J. Noda, "Optical properties of titanium-diffused LiNbO₃ strip waveguides and their coupling-to-a-fiber characteristics," *Appl. Opt.*, vol. 19, no. 4, pp. 591–597, 1980.

[21] A. Yi-Yan, "Index instabilities in proton-exchanged LiNbO₃ waveguides," *Appl. Phys. Lett.*, vol. 42, no. 8, pp. 633–635, 1983.

[22] P. Rabiei, J. Ma, S. Khan, J. Chiles, and S. Fathpour, "Heterogeneous lithium niobate photonics on silicon substrates," *Opt. Express*, vol. 21, no. 21, pp. 25573–25581, 2013.

[23] A. Rao *et al.*, "Heterogeneous microring and Mach-Zehnder modulators based on lithium niobate and chalcogenide glasses on silicon," *Opt. Express*, vol. 23, no. 17, pp. 22746–22752, 2015.

[24] A. Rao *et al.*, "High-performance and linear thin-film lithium niobate Mach-Zehnder modulators on silicon up to 50 GHz," *Opt. Lett.*, vol. 41, no. 24, pp. 5700–5703, 2016.

[25] A.Rao *et al.*, "Second-harmonic generation in periodically-poled thin film lithium niobate wafer-bonded on silicon," *Opt. Express*, vol. 24, no. 26, pp. 29941–29947, 2016.

[26] A. Rao *et al.*, "Second-harmonic generation in single-mode integrated waveguides based on mode-shape modulation," *Appl. Phys. Lett.*, vol. 110, 2017, Art. no. 111109.

[27] A. Honardoost *et al.*, "Cascaded integration of optical waveguides with third-order nonlinearity with lithium niobate waveguides on silicon substrates," *IEEE Photon. J.*, vol. 10, no. 3, Jun. 2018, Art. no. 4500909.

[28] I. Krasnokutska, J. Tambasco, X. Li, and A. Peruzzo, "Ultra-low loss photonic circuits in lithium niobate on insulator," *Opt. Express*, vol. 26, no. 2, pp. 897–904, 2018.

[29] M. Zhang, C. Wang, R. Cheng, A. Shams-Ansari, and M. Loncar, "Monolithic ultra-high-Q lithium niobate microring resonator," *Optica*, vol. 4, no. 12, pp. 1536–1537, 2018.

[30] A. Rao *et al.*, "Highlly efficient nonlinear integrated photonics in ultra-compact periodically-poled lithium niobate on silicon," in *Proc. OSA Frontiers Opt. Annu. Meeting*, Washington, DC, USA, 2018, Paper JTu3A.59.

[31] L. Cao, A. Aboketaf, Z. Wang, and S. Preble, "Hybrid amorphous silicon (a-Si:H)-LiNbO₃ electro-optic modulator," *Opt. Commun.*, vol. 330, pp. 40–44, 2014.

[32] L. Chen, J. Chen, J. Nagy, and R. M. Reano, "Highly linear ring modulator from hybrid silicon and lithium niobate," *Opt. Express*, vol. 23, no. 10, pp. 13255–13264, 2015.

[33] A. J. Mercante, P. Yao, S. Shi, G. Schneider, J. Murakowski, and D. W. Prather, "110 GHz CMOS compatible thin film LiNbO₃ modulator on silicon," *Opt. Express*, vol. 24, no. 14, pp. 15590–15595, 2016.

[34] S. Jin, L. Xu, H. Zhang, and Y. Li, "LiNbO₃ thin-film modulators using silicon nitride surface ridge waveguides," *IEEE Photon. Technol. Lett.*, vol. 28, no. 7, pp. 736–739, Apr. 2016.

[35] L. Cai, Y. Kang, and H. Hu, "Electric-optical property of the proton exchanged phase modulator in single-crystal lithium niobate thin film," *Opt. Express*, vol. 24, no. 5, pp. 4640–4647, 2016.

[36] C. Wang, M. Zhang, B. Stern, M. Lipson, and M. Loncar, "Nanophotonic lithium niobate electro-optic modulators," *Opt. Express*, vol. 26, no. 2, pp. 1547–1555, 2018.

[37] P. O. Weigel *et al.*, "Bonded thin film lithium niobate modulator on a silicon photonics platform exceeding 100 GHz 3-dB electrical modulation bandwidth," *Opt. Express*, vol. 26, no. 18, pp. 23728–23739, 2018.

[38] A. J. Mercante, S. Shi, P. Yao, L. Xie, R. M. Weikle, and D. W. Prather, "Thin film lithium niobate electro-optic modulator with terahertz operating bandwidth," *Opt. Express*, vol. 26, no. 11, pp. 14810–14816, 2018.

[39] C. Wang *et al.*, "100-GHz low voltage integrated lithium niobate modulators," in *Proc. Conf. Lasers Electro-Opt.*, 2018, Paper SM3B.4.

[40] A. Rao, and S. Fathpour, "Compact lithium niobate electrooptic modulators," *IEEE J. Sel. Top. Quantum Electron.*, vol. 24, no. 4, pp. 1–14, Jul./Aug. 2018.

[41] K. Kubota, J. Noda, and O. Mikami, "Travelling wave optical modulator using a directional coupler LiNbO₃ waveguide," *IEEE J. Quantum Electron.*, vol. 16, no. 7, pp. 754–760, Jul. 1980.

[42] G. K. Gopalakrishnan and W. K. Burns, "Performance and modeling of resonantly enhanced LiNbO₃ modulators for low-loss analog fiber-optic links," *IEEE Trans. Microw. Theory Techn.*, vol. 42, no. 12, pp. 2650–2656, Dec. 1994.

[43] H. Chung, W. S. C. Chang, and E. L. Adler, "Modeling and optimization of traveling-wave LiNbO₃ interferometric modulators," *IEEE J. Quantum Electron.*, vol. 27, no. 23, pp. 608–617, Mar. 1991.

[44] J. M. Liu, *Photonic Devices*. Cambridge, U.K.: Cambridge Univ. Press, 2005.

[45] D. M. Pozar, *Microwave Engineering*, 4th ed. Hoboken, NJ, USA: Wiley, 2012.

[46] R. Garg, I. Bahl, and M. Bozzi, *Microstrip Lines and Slotlines*, 3rd ed. Norwood, MA, USA: Artech House, 2013.

[47] E. Chen, and S. Y. Chou, "Characteristics of coplanar transmission lines on multilayer substrates: Modeling and experiments," *IEEE Trans. Microwave Theory Techn.*, vol. 45, no. 6, pp. 939–945, Jun. 1997.

[48] G. Chione *et al.* "Microwave modeling and characterization of thick coplanar waveguides on oxide-coated lithium niobate substrates for electrooptical applications," *IEEE Trans. Microw. Theory Techn.*, vol. 47, no. 12, pp. 2287–2293, Dec. 1999.

[49] J. Baker-Jarvis, M. D. Janezic, B. Riddle, C. L. Holloway, and N. Paulter, "Dielectric and conductor-loss characterization and measurements on electronic packaging materials," NIST, Gaithersburg, MD, USA, Tech. Note 1520, 2001.

[50] C. Cochard, T. Spielmann, N. Bahlawane, A. Halpin, and T. Granzow, "Broadband characterization of congruent lithium niobate from mHz to optical frequencies," *J. Phys. D: Appl. Phys.*, vol. 50, no. 36, 2017, Art. no. 36LT01.

[51] W. B. Westphal and A. Sils, "Dielectric constant and loss data," Massachusets Inst. Technol., Cambridge, MA, USA, Tech. Rep. AFML-TR-72-39, 1972.

[52] G. Chione, "A CAD-oriented analytical model for the losses of general asymmetric coplanar lines in hybrid and monolithic MICs," *IEEE Trans. Microw. Theory Techn.*, vol. 41, no. 9, pp. 1499–1510, Sep. 1993.

Amirmahdi Honardoost (S'10) received the B.Sc. degree in electrical engineering from Shahid Beheshti University, Tehran, Iran, in 2012, and the M.Sc. degree in electrical engineering from the University of Central Florida, Orlando, FL, USA, in 2016. He is currently working toward the Ph.D. degree with CREOL, the College of Optics and Photonics, University of Central Florida, Orlando, FL, USA. He is a coauthor of 15 journal and conference papers. His research includes high-speed compact electrooptic modulators, second-order nonlinear optical frequency converters, and monolithic integration of optical waveguides with thin-film lithium niobate.

Reza Safian received the Ph.D. degree in electrical engineering from the University of Toronto, Toronto, ON, Canada, in 2008. He joined the faculty of the Department of Electrical and Computer Engineering with the Isfahan University of Technology in 2008, where he was involved in the field of terahertz and millimeter wave imaging and guided-wave optoelectronics. He was a visiting researcher with CREOL, the College of Optics and Photonics, University of Central Florida, in 2017, working on the wideband integrated electrooptic modulators. In 2018, he joined the IMEC R&D, nano electronics and digital technologies in Florida, where he is working in the field of terahertz imaging. He is a coauthor of more than 100 papers in journals and conference proceedings.

Ashutosh Rao (S'16) received the B.Tech. and M.Tech. degrees in engineering physics from the Indian Institute of Technology Bombay, Mumbai, India, in 2013, and the Ph.D. degree in optics from CREOL, the College of Optics and Photonics, University of Central Florida, Orlando, FL, USA, in 2018. He is a coauthor of 35 journal and conference papers. His research has included demonstrations of high-speed electrooptic modulators, second-order nonlinear optical frequency converters, and photon-pair generation in thin-film lithium niobate waveguides.

Sasan Fathpour (S'01–M'04–SM'13) received the Ph.D. degree in electrical engineering from the University of Michigan, Ann Arbor, MI, USA, in 2005. He is currently a Professor with CREOL, the College of Optics and Photonics, University of Central Florida, Orlando, FL, USA. He joined the Electrical Engineering Department, University of California, Los Angeles, Los Angeles, CA, USA, as a Postdoctoral Fellow and joined the CREOL faculty in 2008. He is the coeditor of a book entitled *Silicon Photonics for Telecommunications and Biomedicine*, published by CRC Press in 2012, and a coauthor of about 160 journal and conference papers, book chapters, and patents. His current research interests include heterogeneous integrated photonics, nonlinear integrated optics, silicon photonics, and nonconventional optical waveguide platforms for mid-wave infrared and other applications.

Prof. Fathpour was a recipient of the ONR Young Investigator Award (2013) and the NSF CAREER Award (2012). He is a Fellow of OSA, the Optical Society of America, and a Senior Member of SPIE.